

Dual-energy electron beams from a compact laser-driven accelerator

J. Wenz^{1,2,7}, A. Döpp^{1,2,7*}, K. Khrennikov^{1,2,7}, S. Schindler^{1,2}, M. F. Gilljohann^{1,2}, H. Ding^{1,2}, J. Götzfried¹, A. Buck^{1,2}, J. Xu^{2,6}, M. Heigoldt^{1,2}, W. Helml^{1,3,4}, L. Veisz^{1,2,5} and S. Karsch^{1,2*}

Ultrafast pump-probe experiments open the possibility to track fundamental material behaviour, such as changes in electronic configuration, in real time. To date, most of these experiments are performed using an electron or a high-energy photon beam that is synchronized to an infrared laser pulse. Entirely new opportunities can be explored if not only a single, but multiple synchronized, ultrashort, high-energy beams are used. However, this requires advanced radiation sources that are capable of producing dual-energy electron beams, for example. Here, we demonstrate simultaneous generation of twin-electron beams from a single compact laser wakefield accelerator. The energy of each beam can be individually adjusted over a wide range and our analysis shows that the bunch lengths and their delay inherently amount to femtoseconds. Our proof-of-concept results demonstrate an elegant way to perform multi-beam experiments in the future on a laboratory scale.

Understanding the dynamics of materials on the timescale of electronic, atomic and molecular motion is one of the grand challenges of contemporary physics, chemistry and biology¹. A particularly useful tool to study these phenomena are pump-probe experiments, where a process is triggered using a pump pulse and its temporal evolution is subsequently examined using a probe pulse. Importantly, the properties of the radiation pulses dictate which type of systems can be studied with this method. Commonly available short-pulse infrared lasers are mostly used as a pump to excite or manipulate weakly bound electronic² and magnetic³ states, to ionize⁴ or to heat a target⁵. The induced dynamics of the system are probed with a short electron or photon beam. For instance, electron⁶ or X-ray⁷ diffraction are sensitive to atomic arrangement, while X-ray absorption spectroscopy⁸ is a particularly useful tool to study complex systems, because materials exhibit well-distinguishable transitions in the X-ray regime resulting in element selectivity⁹.

In the case of processes governed by atomic motion, the vibrational period (~100 fs) needs to be resolved¹⁰. So far, the required femtosecond X-ray pulses for pump-probe experiments can only be provided at accelerator-based light sources¹¹, using either femto-slicing beamlines¹² or free-electron lasers^{13,14}. In the near future, laser-driven accelerators¹⁵ could serve as complementary or alternative femtosecond radiation sources. Their ultrashort¹⁶ megaelectronvolt-to-gigaelectronvolt-scale^{17,18} electron bunches are already being used to provide femtosecond photon beams in the terahertz¹⁹, ultraviolet²⁰, X-ray^{21,22} and gamma-ray²³ regimes. While laser-driven X-ray sources were initially limited to performing basic radiography^{24,25}, recent experiments have started to take advantage of the sources' temporal resolution in pump-probe studies of warm dense matter²⁶ and laser-driven shock waves²⁷.

An entirely new class of experiments becomes available when short-wavelength pulses are used for both pumping and probing^{28–30}. In this dual-colour operation it is, for instance, possible to combine direct stimulation of core state transitions with the

sensitivity of the above-mentioned X-ray probing techniques. Motivated by this perspective, the free-electron laser community has been actively developing a number of different schemes for dual-colour operation³¹, ranging from multiple seed pulses³², over staggered undulator magnets³³, to dual-energy electron bunches³⁴. Dual-energy electron bunches have the great advantage that they require no modifications to the undulator beamline and the pulse delay can be adjusted with magnetic chicanes³⁵. But even in this case, the separation of both electron beam energies is at the percent level. Accordingly, the X-ray energy separation is also at a percent level for this approach, while up to 30% can be reached using staggered undulators. Furthermore, access to free-electron lasers is restricted to a few experimental groups per year, and the demand of round-the-clock operation severely limits their flexibility in terms of setup changes between beam times. Thus, it is very difficult to explore new or unconventional experimental configurations such as dual-colour operation. A complementary compact source of widely tunable, ultrashort, dual-energy electron beams is therefore highly desirable to pursue high-energy pump-probe experiments of molecular or atomic systems.

Here we demonstrate the generation of such twin beams from a laser wakefield accelerator (LWFA) driven by a 100-TW-class Ti:Sa laser. The energy of the two beams can be adjusted over a wide range and our analysis shows that both duration and temporal separation of the beams is of the order of 10 fs. Given the large energy difference, the beams should be suitable for timing adjustments in magnetic chicanes. We also discuss the performance of dual-colour photon sources derived from these twin beams and present an implementation in an all-optical Compton source.

Comparison of monoenergetic electron beam sources

Over the past decade, a variety of techniques have been introduced to generate narrow bandwidth electron beams using an LWFA³⁶. Passive injection schemes such as self-injection³⁷ and ionization-

¹Ludwig-Maximilians-Universität München, Garching, Germany. ²Max Planck Institut für Quantenoptik, Garching, Germany. ³Technische Universität Dortmund, Dortmund, Germany. ⁴Technische Universität München, Garching, Germany. ⁵Department of Physics, Umea University, Umea, Sweden. ⁶Present address: State Key Laboratory of High Field Laser Physics, Shanghai Institute of Optics and Fine Mechanics, Chinese Academy of Sciences, Shanghai, China. ⁷These authors contributed equally: J. Wenz, A. Döpp, K. Khrennikov. *e-mail: a.doep@physik.uni-muenchen.de; stefan.karsch@mpq.mpg.de

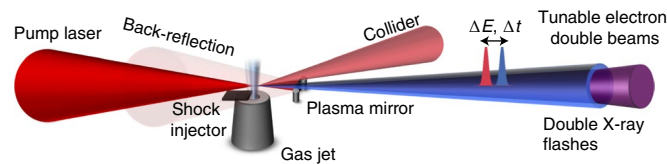


Fig. 1 | Dual-energy femtosecond electron and X-ray source. Using a single high-power laser system, two injection events are triggered by shock-front and colliding-pulse injection, resulting in the generation of spectrally distinct electron beams with energy difference ΔE and femtosecond delay Δt . In a second experiment, these electrons are used for radiation generation using Compton backscattering following the reflection of the pump laser on a plasma mirror (Mylar tape).

induced injection³⁸ remain the most popular, due to their simplicity to implement. For self-injection, electron spectra with several peaks have occasionally been observed in experiments (see, for example, ref.³⁹), yet these are typically the result of injection into different wakefield periods⁴⁰ and are neither stable nor tunable. To generate tunable twin beams, it is necessary to trigger the electron-injection process at controlled positions, which is hardly possible using these methods. One solution could be the use of dual-colour laser pulses⁴¹, yet this technique still awaits demonstration. Instead, experimentally more challenging active electron injection techniques are required, among which optical injection⁴² and shock-front injection^{43,44} are arguably the most promising methods. Optical injection adds a second colliding pulse to the setup to create favourable trapping conditions during the interaction with the drive pulse⁴². While injection may be caused by several different mechanisms^{45–47}, depending on the exact conditions, all variants of optical injection produce ultrashort, quasi-monoenergetic electron bunches, whose energy can be adjusted by moving the collision point along the plasma channel. Shock-front injection is an injection method purely based on plasma density tailoring that uses a sharp blade or wafer to create a supersonic shock in the gas flow of the target. At this shock front, a rapid transition from high plasma density (n_1) to low density (n_0) occurs, which leads to a sudden increase of the plasma wavelength λ_p . Accordingly, the laser wakefield expands, which temporarily facilitates trapping of electrons. As for colliding-pulse injection, the injection position is tunable; in this case, by moving the blade with respect to the gas jet.

We have compared both techniques in experiments with the ATLAS Ti:Sa laser system, using de Laval gas nozzles to create a supersonic gas flow suitable for shock-front injection (cf. Methods and Fig. 1). Figure 2 shows the spectra of the electron beams obtained using both shock-front and colliding-pulse injection techniques separately, albeit with the same driving laser, focusing geometry, gas nozzle and gas density. The beams exhibit similar properties and have, for an LWFA, a high stability, reproducibility and tuning range. The use of the shock-front injector results in a higher spectral charge density compared with the optical scheme, which is, however, paired with a slightly increased energy bandwidth. Single-shot energy spectra are shown in Supplementary Fig. 1.

The beam energy scales approximately linearly with the acceleration distance. This is expected as the acceleration length $L_{\text{acc}} < 0.7 \text{ mm}$ is much smaller than the dephasing length of $L_d \approx 5 \text{ mm}$, which we estimate using the scalings from Lu et al.⁴⁸. We find that the average acceleration field experienced by shock-injected beams is $(74 \pm 6) \text{ GV m}^{-1}$, while we measure an acceleration gradient of $(62 \pm 5) \text{ GV m}^{-1}$ for optically injected beams. The difference between gradient measurements seems to be caused by beam loading effects, because the beam charge is not constant over the scan and electron bunches do not necessarily have the same charge density. The beam loading effects are manifested by the diminishing bunch charge and hence higher energy when the blade is close to the gas jet entrance (where n_1/n_0 is smaller in the case of shock-front injection). In contrast, the beam charge for colliding-pulse injection

increases towards the beginning of the jet, which is expected to lower the final beam energy. Here, the bunch charge is related to the product of the vector potentials of collider and main beam⁴⁹, so the increasing charge is likely a result of the relative focusing between the two lasers. For both measurements the divergence of the electron beams scales as theoretically expected with $\gamma^{-3/4}$, where γ is the relativistic factor of the electron beam⁵⁰.

Generation of dual-energy electron beams

In a next step, we integrated both injection configurations into a single setup, which allowed us to use them simultaneously. As moving the shock-front position perturbs the beginning of the gas jet, we moved the blade to a fixed position that continuously produced electron beams with a peak energy of about 40 MeV. Then, the colliding pulse is activated and the entire jet (including the blade that forms the shock) is moved along the laser axis with respect to the collision position. It should be noted that this also changes the intensity of the laser at the shock front, leading to a decrease in the bunch charge as the target is moved closer to the focusing parabola (cf. Supplementary Fig. 3).

By changing the relative position of shock and pulse collision, we observe three distinct behaviours (cf. Fig. 3a). When the collision occurs before the shock, the electron beam spectra show only a single monoenergetic peak. This signal is indistinguishable from sole shock-front injection, indicating that the optical injection mechanism is suppressed. With the collision occurring close to the density transition, we observe that the energy of the monoenergetic feature suddenly decreases. As this effect is accompanied by an increase in beam charge, it resembles the situation studied by Fubiani et al.⁵¹, where colliding pulse injection is augmented by a density down-ramp, and the enhanced charge causes an energy reduction via beam loading. Then, as we move the collision point further outwards onto the density plateau, two separate monoenergetic peaks form. The first is very similar to shock-front injection without the collision pulse, and is therefore still attributed to shock-front injection. The second, low-energy peak could be adjusted between 10 and 25 MeV by varying the collision position and is hence the result of colliding-pulse injection. We also notice that both charge and energy of the optically injected electrons are lower than for the reference case without a shock (cf. Supplementary Fig. 2). As we discuss below, this effect is attributed to beam loading caused by the shock-injected bunch, which weakens the accelerating fields during injection and subsequent acceleration.

To understand the physics underlying the different operation regimes of the accelerator, we have performed a series of quasi-three-dimensional particle-in-cell (PIC) simulations. The results, which are depicted in Fig. 3b–d, accurately reproduce the experimentally observed behaviour. Before the shock, the plasma density is increasing and hence the plasma wavelength decreases. Analogous to the plasma wave expansion during shock-front injection, this causes a wake contraction at a velocity $v_{\text{ramp}} \propto d\lambda_p/dt$. Electron injection and acceleration only occur if the electrons can reach a velocity close to the wake's phase velocity $v_\phi \approx v_g - v_{\text{ramp}}$, where v_g is the group velocity

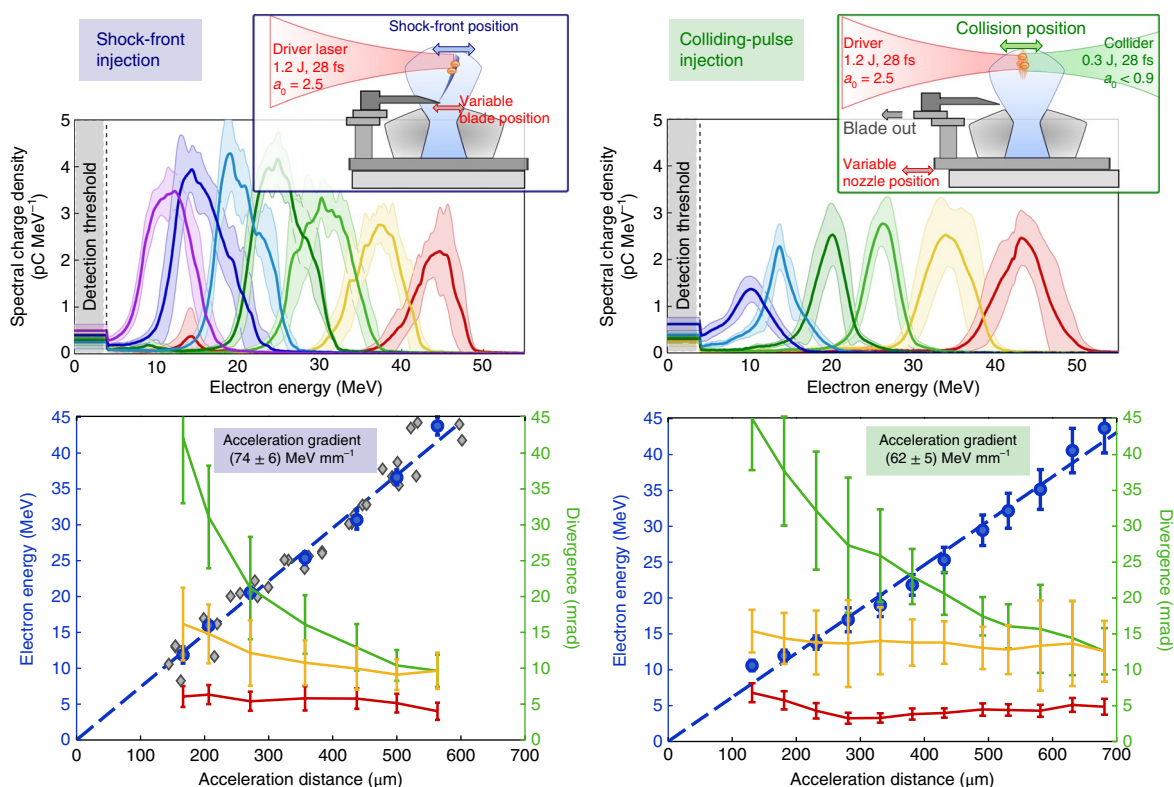


Fig. 2 | Experimental tuning of electron beam energy using shock-front and colliding-pulse injection schemes. Insets: Sketches of the basic setup. Tuning of the electron energy is obtained by variation of the acceleration length by adjusting the position of the blade (left) or collision position (right) within the gas flow. Top: Averaged energy spectra of selected ten shots for different acceleration length settings. Shaded areas show the shot-to-shot fluctuation range and colours are arbitrary chosen to help to distinguish the individual settings. Bottom: Resulting beam characteristics. Blue dots represent the averaged peak energy of the bunch, with error bars showing the root mean square stability over the complete scan. Red curves depict the average spectral widths (FWHM) for each energy setting. Green (yellow) curves show the (normalized by $\gamma^{3/4}$, see main text) beam divergence. Energy spectra of individual shots of the whole experimental run can be found in the Supplementary Information.

of the laser. During the upramp ($v_{\text{ramp}} < 0$), the phase velocity is increased and can even reach superluminal speed⁵². So, despite electrons gaining momentum after the pulse collision, injection is inhibited during this phase. The situation changes close to the density peak of the shock, where the relaxed injection conditions allow the pre-accelerated electrons to get trapped inside the second wakefield period.

Once the pulse collision occurs at the density downramp, the injection behaviour changes. A single injection event is observed, with increased charge and lower final beam energy. Simulations suggest that we are operating in the regime of optical transverse injection, where the pulse collision causes a rapid contraction and re-expansion of the wakefield⁴⁷. Accordingly, this regime can be understood as optically assisted shock-front injection. As this combined injection occurs inside the same plasma cavity, the increased charge causes beam loading and thus lowers the energy gain.

Moving the collision point towards the end of the jet, the two injection events separate, resulting in two distinct peaks in the spectrum. In the simulations, we observe a full-width at half-maximum (FWHM) duration of 12–14 fs for the high-energy bunch, while the duration of the second beam varies from 4–12 fs. Note that this is a higher value than typically observed in experiments^{16,52,53}, but similar to other simulation results, for example, on colliding-pulse injection¹⁶. The varying duration of the second electron bunch can be explained as a result of beam loading of the first beam, which prohibits injection in its vicinity. This can also be seen in the shape of the simulated longitudinal wakefields (cf. Fig. 3d). Accordingly, the beam charge and energy of the optically injected beam are reduced

compared with pure colliding-pulse injection for injection very close to the shock-injected bunch.

The temporal delay Δt between the peaks of both femtosecond electron bunches is determined by two factors—the duration of the first beam and the amount of dephasing that occurs between the injection events. In simulations, we observe a robust temporal synchronization, which approximately follows $\Delta t \approx \tau_{\text{shock}} + (1 - v_g/c_0) \Delta x/c_0$, where c_0 is the speed of light in vacuum, τ_{shock} is the duration of the shock-injected beam and Δx is the distance between shock and pulse collision (see Supplementary Information for more details). In practical numbers, this means that Δt increases with the injection position by $3 \text{ fs} \cdot n_e [10^{18} \text{ cm}^{-3}] \cdot \Delta x [\text{mm}]$, n_e being the plasma density. Accordingly, the timing jitter between both beams is also very small, as any initial jitter Δt_{jitter} between main pulse and collider results in a much smaller timing difference of approximately $(1 - v_g/c_0) \Delta t_{\text{jitter}}$.

Hence, we have demonstrated dual-energy beam generation in an LWFA and simulations accurately reproduce the behaviour observed in experiments. Our analysis shows that the electron beam not only exhibits distinctive energy peaks, but also consists of two femtosecond electron bunches with femtosecond delay. Simulations strongly suggest that this delay can be easily modified on a femtosecond scale by changing the distance between injection events, which still needs to be verified experimentally in future. Hence, the results are extremely promising for a variety of applications in ultrafast science. For instance, they could allow the use of femtosecond electron diffraction of the second bunch⁵⁴ to study femtosecond radiolysis induced by the first⁵⁵. Laboratory-scale dual-colour photon

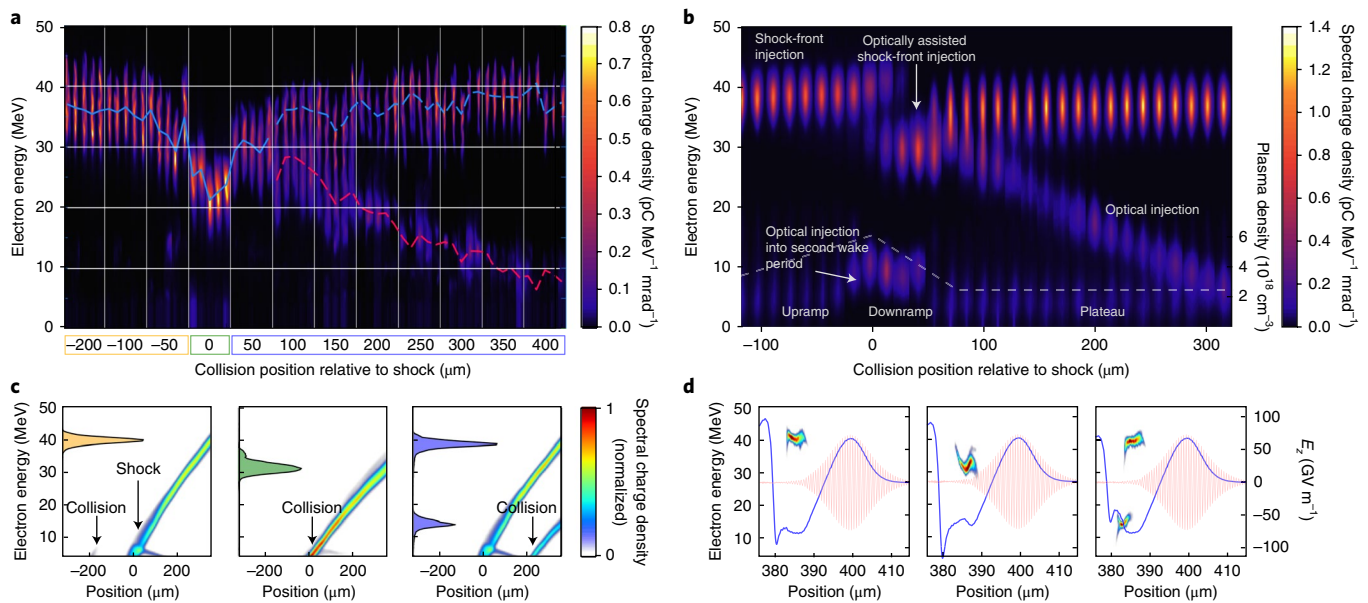


Fig. 3 | Demonstration of dual-energy electron beams and PIC simulations. **a**, Individual electron spectra for different settings of the optical collision position and fixed shock front. Positions are referenced to the shock front. For negative collision position settings, that is, in the density upramp, no optically injected electrons are observed. Collision at 0 mm shows enhanced injection, while the peak energy (dashed blue line) is reduced due to beam loading. At positive values: demonstration of the tunable optically injected beam behind the leading electron beam from the shock-front injection scheme (peak energy shown as red line). **b**, PIC simulations of the experiment, clearly showing the same three distinct regimes for collision in the upramp, downramp and on the plateau. **c**, Evolution of the electron energy spectrum in the first bubble for the three cases along the jet. The final spectrum is indicated along the left vertical axis, with filling colours corresponding to the individual cases (frames of the relative position labels) in **a**. The evolution of the spectrum during acceleration is plotted as a two-dimensional false-colour plot in each figure. For a collision in the upramp, electrons are initially accelerated, but are quickly lost due to the superluminal phase velocity of the wake. If the collision occurs during the downramp, the amount of injected charge increases, and for collision on the plateau two separate beams emerge. **d**, Longitudinal phase space (false colour), on-axis plasma field lineouts (blue) and laser field (red) at the end of the accelerator for each case.

sources derived from the electron beams may pose even greater interest, as we will discuss in the following.

Applicability as secondary radiation source

As mentioned earlier, LWFA can be combined with a number of radiation mechanisms to generate femtosecond photon beams. In the case of a dual-energy electron beam, each electron bunch will emit radiation at different wavelengths. For magnetic undulators or Thomson sources, the fundamental wavelength of the emitted photons will be $\lambda' = \frac{\lambda_0}{\kappa\gamma^2} \left(1 + \frac{1}{2\kappa^2}\right)$, where γ is the Lorentz factor of the bunches. In a magnetic undulator, the fundamental wavelength $\lambda_0 \sim \text{cm}$, $\kappa = 2$ and the undulator strength parameter $K = \frac{eB\lambda_0}{2\pi m_e c}$, where B is the magnetic field. For Thomson sources, also frequently referred to as inverse Compton sources, the peak angular deflection is determined by the normalized vector potential a_0 instead of K . Furthermore, the Doppler upshift depends on the collision angle ϕ , that is $\kappa \simeq 2(1 - \cos\phi)$. Due to the small oscillation length $\lambda_0 \sim \mu\text{m}$, inverse Compton sources can provide kiloelectronvolt-scale radiation using $>10\text{MeV}$ electrons²¹, whereas a comparable undulator source would require gigaelectronvolt-scale electron energies. A Compton source based on the presented dual-energy electron beams would therefore emit dual-colour X-rays in the multi-kiloelectronvolt regime⁵⁶. As proposed by Kalmykov et al.^{57,58}, a Compton source combined with a laser-accelerated gigaelectronvolt-scale electron twin-beam could even provide gamma-ray twin pulses.

Operating an LWFA at higher energies generally reduces the electron beam divergence and gives access to a larger range of useful secondary sources. We have therefore repeated the experiment with

an upgraded laser and longer gas jets, which allowed us to increase the electron energy by almost an order of magnitude. Electrons from shock-front injection routinely reached 350 MeV, while the energy of the optically injected beam was tuned from 50 MeV to 200 MeV. Figure 4a shows an example of a dual-energy beam generated in this new experiment, which has two quasi-monochromatic peaks at 185 MeV and 343 MeV. Furthermore, the beam divergence is reduced to 1 mrad. Simulations show that these electron beams would be suitable to generate extreme ultraviolet radiation (using magnetic undulators, Fig. 4b) or even gamma-rays (based on Compton backscattering, Fig. 4c). Importantly, the temporal profile of the backscattered radiation will be determined by the electron beam⁵⁹. For weak undulator parameters ($K < 1$), the radiation from both electron bunches is spectrally distinguishable, while the emission from nonlinear Compton scattering is more broadband and partly overlaps. The latter could be improved using chirped scattering pulses⁶⁰. As discussed previously, simulations predict that the laser-accelerated dual-energy electron beams exhibit a clear temporal structure, with the high-energy bunch arriving first, followed by the second femtosecond electron bunch 10–20 fs later. The radiation emitted by these electrons will therefore also take the form of two femtosecond bursts.

As a proof-of-principle experiment, we have performed inverse Compton scattering with both single and dual-energy electron beams (Fig. 5). For this, we integrated a plasma mirror into the experimental setup that retro-reflects the drive laser pulse of the LWFA onto the trailing electrons⁶¹. The upper edge of the plasma mirror was placed close to the laser axis, allowing the colliding beam to pass over it (cf. Fig. 5). In this experiment, the 350 MeV beam from shock-front injection had a comparably low charge of

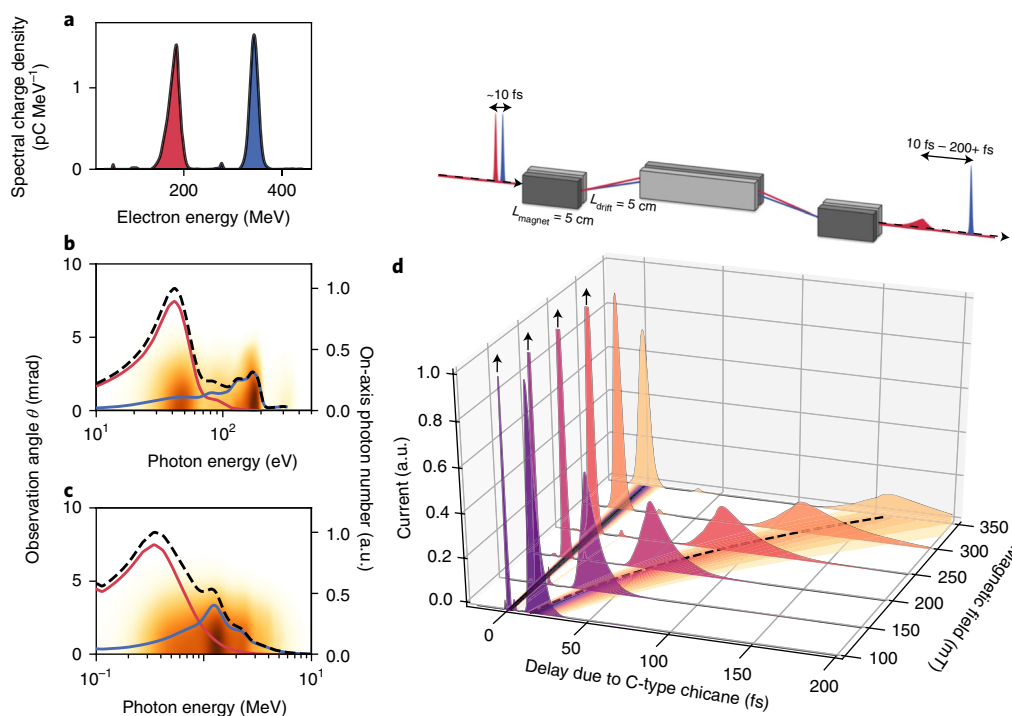


Fig. 4 | Proposed radiation source and timing control based on dual-energy electron beams. **a**, Electron beam spectrum obtained using the upgraded ATLAS-300 laser, exhibiting two peaks at 185 MeV (red) and 343 MeV (blue), with a FWHM energy spread of 13% and 6%, respectively. **b,c**, Simulated synchrotron emission in a magnetic undulator ($\lambda_0 = 5$ mm, $K = 0.55$ and $n_{\text{periods}} = 60$; **b**) and an all-optical Compton source ($\lambda_0 = 800$ nm, $a_0 = 1.5$, $\Delta t = 30$ fs; **c**). Dashed lines show the combined on-axis photon number whereas red and blue lines follow the signal emitted by the respective electron bunches. The underlying colour map shows the angularly resolved radiation emission. **d**, The delay the electron beams would experience in a C-type magnetic chicane with drift length $L_{\text{drift}} = 5$ cm and magnet length $L_{\text{magnet}} = 5$ cm for various magnetic field strengths. The initial bunch duration and delay are estimated to amount to $\lesssim 10$ fs.

(25 ± 10) pC and we observed a 2.3 mrad FWHM photon beam on the detector. Activating the collision pulse added a quasi-monochromatic bunch at 210 MeV with (39 ± 10) pC charge to the electron beam, while the shock-injected beam remained unchanged with a charge of (27 ± 9) pC. Under these conditions, the peak signal on the scintillator was 45% higher and the beam divergence increased to 2.8 mrad, showing clearly the contribution of the second electron bunch. Simulations based on the measured electron beams predict a similar signal gain (57%) and reproduce the beam profile (see line-outs in Fig. 5). The expected radiation spectrum is similar to Fig. 4c.

Therefore, the presented dual-energy electron source has great potential to provide dual-colour X-rays. However, before these beams can reliably be used for any application, issues such as beam transport need to be considered. In particular, the transport of beams with large energy separation will require higher-order magnetic optics or beam optics with low chromaticity (see also Supplementary Information).

The delay between both electron bunches, and hence all derived radiation sources, is determined by the injection mechanism. In our measurements, we reproducibly observe the emission of injection radiation⁶² at the shock and collision positions. As discussed above, this will result in essentially jitter-free delay between both beams, which are accelerated within the same ion cavity. But for many applications, such as already mentioned pump-probe measurements or also plasma wakefield acceleration⁶³, it is also important to be able to fine tune the delay of the electron twin bunches. Given the large energy difference achieved with this source, the bunch separation naturally increases over a propagation distance x due to velocity delay by $\Delta t \approx \left(\frac{1}{\gamma_1^2} - \frac{1}{\gamma_2^2} \right) \frac{x}{2c_0}$. For the electron beam from Fig. 4a, this evaluates to $\Delta t \approx 9$ fs $\times x$ [m]. However, at the same time,

the entire beam will also experience temporal broadening due to its divergence. While temporal broadening dominates for beams of large divergence, we concentrate in the following on 1 mrad electron beams, as generated in the last experiment. Here the divergence-induced pulse broadening remains on the order of 1–2 fs for metre-scale propagation lengths and is therefore negligible.

Similar to twin-beam approaches at free-electron lasers, even longer delays can be achieved using magnetic chicanes. Again, the large energy difference is beneficial, because it allows the electron bunch delay to be adjusted over short distances. As shown in Fig. 4d, a 30-cm-long chicane with modest magnetic fields (100–350 mT) would be sufficient to induce a delay ranging from a few femtoseconds to more than 200 fs, which is the timing range required for pump-probe measurements of atomic and molecular systems. In this regime, the initial delay and duration of the electron beams (~ 10 fs) is also negligible. Nonetheless, the exact duration and delay would have to be determined in future experiments to increase the resolution from ~ 10 fs to about 1 fs. While the finite energy spread of each electron bunch will lead to pulse lengthening (especially for the low-energy beam), the bunch length remains much shorter than the delay. This is a critical criterion for applications such as sequential imaging or molecular excitation and probing (see Supplementary Information for more details on potential applications).

Last, it should be mentioned that the high-energy pulse always arrives first in our configuration. This is due to the injection and dephasing process in an LWFA and it would be preserved in the chicane setup, as well. The time-energy correlation can to some extent be compensated within the LWFA itself⁶⁴, but a complete inversion will be limited by pump depletion and other related processes that occur at the end of the accelerator. Still, the presented time-energy correlation is suitable for many applications such as the ones mentioned above.

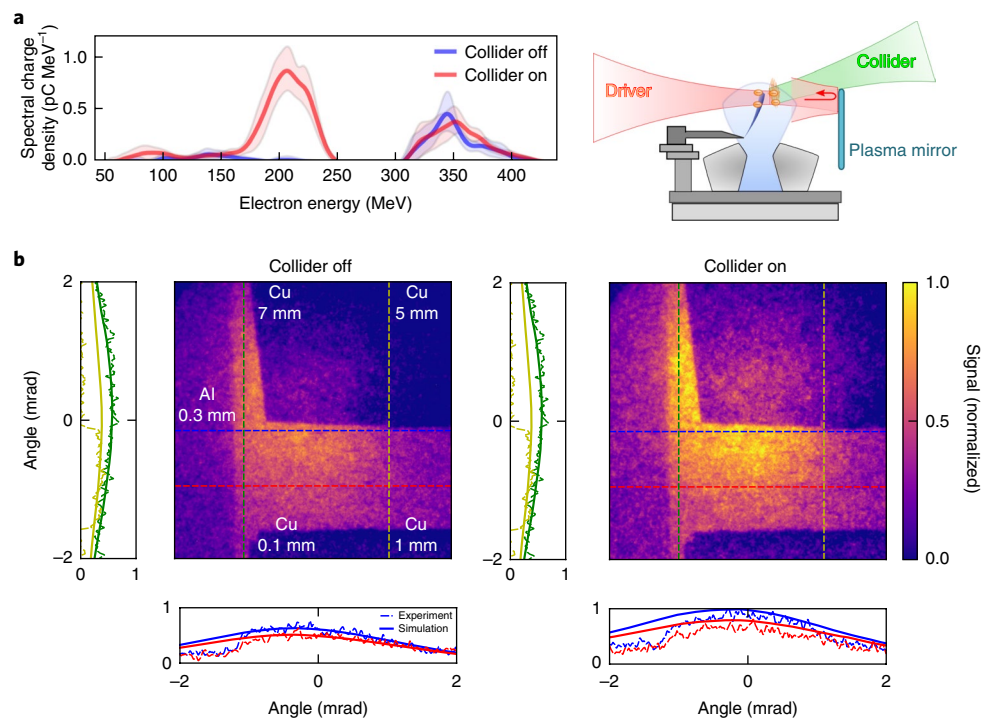


Fig. 5 | Radiation generation using an all-optical Compton source. **a**, Sketch of the setup, consisting of a shock-front injector, colliding-pulse injector and plasma mirror (right) and average electron beam spectrum over ten shots (left). **b**, Observed radiation signal from Compton backscattering (ten shot average) for a single-energy electron beam (left) and enhanced signal using a dual-energy beam (right). Both images are normalized to the peak signal level of the dual-beam case, at identical camera settings. Note that darker areas are covered with transmission filters (copper or aluminium, see labels in the plot). Lineouts show that both divergence and peak intensity of the measured data (dashed lines) agree within the filter-free areas with the simulated intensity profiles (solid lines) for the same electron beams and a colliding beam with $a_0 = 1.5$.

Conclusions

We have proposed and demonstrated a scheme to generate monoenergetic femtosecond electron twin-beams with tunable energy and delay using a LWFA. The setup can be implemented at any 100-TW-scale laser facility and generates colinear electron beams with largely different energies, while the timing jitter is estimated to be of the order of femtoseconds, which is advantageous compared with, for example, a setup based on two separate LWFAs. The double-bunch structure was successfully produced at maximum energies of 40 MeV and 350 MeV, and in a proof-of-principle experiment the system was combined with an all-optical Compton source.

Our analysis shows the complex interplay of the two different electron injection schemes and we have identified regimes for twin-beam generation as well as a new regime of optically assisted shock-front injection. Further studies may also allow the generation of specific longitudinal charge density profiles to optimize the accelerator performance⁶⁵, probe the beam loading by the first beam⁶⁶ or study plasma wakefield acceleration schemes⁶⁷.

Furthermore, we have presented a detailed discussion of the source's potential as a secondary radiation source. As all laser wakefield sources, the electron beams can be combined with various radiation mechanisms to generate short-wavelength photon beams in the ultraviolet to gamma-ray range. In particular, we propose to use the source for dual-colour pump-probe experiments. Here our approach has many advantages compared to existing dual-colour sources, that is, it is essentially jitter free, the pulse delay can be fine tuned in the femtosecond to picosecond range and it can operate at very large energy separation. At the same time, all electron beams and secondary radiation emission are inherently synchronized to the drive laser system. Hence, this laboratory-scale source would be suitable to study the ultrafast behaviour of complex molecular systems as required for many problems of ultrafast biology⁶⁸, chemistry⁶⁹ and physics⁷⁰.

Online content

Any methods, additional references, Nature Research reporting summaries, source data, statements of data availability and associated accession codes are available at <https://doi.org/10.1038/s41566-019-0356-z>.

Received: 13 August 2018; Accepted: 4 January 2019;
Published online: 18 February 2019

References

- Krausz, F. & Ivanov, M. Attosecond physics. *Rev. Mod. Phys.* **81**, 163–234 (2009).
- Kupitz, C. et al. Serial time-resolved crystallography of photosystem II using a femtosecond X-ray laser. *Nature* **513**, 261–265 (2014).
- Beaurepaire, E., Merle, J. C., Daunois, A. & Bigot, J.-Y. Ultrafast spin dynamics in ferromagnetic nickel. *Phys. Rev. Lett.* **76**, 1–4 (1996).
- Pertot, Y. et al. Time-resolved X-ray absorption spectroscopy with a water window high-harmonic source. *Science* **355**, 264–267 (2017).
- Rousse, A. et al. Non-thermal melting in semiconductors measured at femtosecond resolution. *Nature* **410**, 65–68 (2001).
- Sciaini, G. & Miller, R. J. D. Femtosecond electron diffraction: heralding the era of atomically resolved dynamics. *Rep. Prog. Phys.* **74**, 096101 (2011).
- Cavalleri, A. et al. Tracking the motion of charges in a terahertz light field by femtosecond X-ray diffraction. *Nature* **442**, 664–666 (2006).
- Bressler, C. & Chergui, M. Ultrafast X-ray absorption spectroscopy. *Chem. Rev.* **104**, 1781–1812 (2004).
- Chergui, M. & Collet, E. Photoinduced structural dynamics of molecular systems mapped by time-resolved X-ray methods. *Chem. Rev.* **117**, 11025–11065 (2017).
- Rousse, A., Rischel, C. & Gauthier, J. C. Colloquium: femtosecond X-ray crystallography. *Rev. Mod. Phys.* **73**, 17–31 (2001).
- Bostedt, C. et al. Linac coherent light source: the first five years. *Rev. Mod. Phys.* **88**, 015007 (2016).
- Schoenlein, R. W. et al. Generation of femtosecond pulses of synchrotron radiation. *Science* **287**, 2237–2240 (2000).
- McNeil, B. W. J. & Thompson, N. R. X-ray free-electron lasers. *Nat. Photon.* **4**, 814–821 (2010).

14. Pellegrini, C. X-ray free-electron lasers: from dreams to reality. *Phys. Scr.* **T169**, 014004 (2016).
15. Esarey, E., Schroeder, C. B. & Leemans, W. P. Physics of laser-driven plasma-based electron accelerators. *Rev. Mod. Phys.* **81**, 1229–1285 (2009).
16. Lundh, O. et al. Few femtosecond, few kiloampere electron bunch produced by a laser–plasma accelerator. *Nat. Phys.* **7**, 219–222 (2011).
17. Malka, V. et al. Electron acceleration by a wake field forced by an intense ultrashort laser pulse. *Science* **298**, 1596–1600 (2002).
18. Leemans, W. P. et al. GeV electron beams from a centimetre-scale accelerator. *Nat. Phys.* **2**, 696–699 (2006).
19. Leemans, W. et al. Observation of Terahertz emission from a laser-plasma accelerated electron bunch crossing a plasma-vacuum boundary. *Phys. Rev. Lett.* **91**, 074802 (2003).
20. Fuchs, M. et al. Laser-driven soft-X-ray undulator source. *Nat. Phys.* **5**, 826–829 (2009).
21. Khrennikov, K. et al. Tunable all-optical quasimonochromatic Thomson X-ray source in the nonlinear regime. *Phys. Rev. Lett.* **114**, 195003 (2015).
22. Döpp, A. et al. Stable femtosecond X-rays with tunable polarization from a laser-driven accelerator. *Light Sci. Appl.* **6**, e17086 (2017).
23. Yan, W. et al. High-order multiphoton Thomson scattering. *Nat. Photon.* **11**, 514–520 (2017).
24. Fourmaux, S. et al. Single shot phase contrast imaging using laser-produced betatron X-ray beams. *Opt. Lett.* **36**, 2426–2428 (2011).
25. Kneip, S. et al. X-ray phase contrast imaging of biological specimens with femtosecond pulses of betatron radiation from a compact laser plasma wakefield accelerator. *Appl. Phys. Lett.* **99**, 093701 (2011).
26. Mahieu, B. et al. Probing warm dense matter using femtosecond X-ray absorption spectroscopy with a laser-produced betatron source. *Nat. Commun.* **9**, 3276 (2018).
27. Wood, J. C. et al. Ultrafast imaging of laser driven shock waves using betatron X-rays from a laser wakefield accelerator. *Sci. Rep.* **8**, 11010 (2018).
28. Allaria, E. et al. Two-colour pump–probe experiments with a twin-pulse-seed extreme ultraviolet free-electron laser. *Nat. Commun.* **4**, 2476 (2013).
29. Bencivenga, F. et al. Four-wave mixing experiments with extreme ultraviolet transient gratings. *Nature* **520**, 205–208 (2015).
30. Ferrari, E. Seeded multicolor FEL pulses: status and future plans. *Synchrotron Radiat. News* **29**, 4–9 (2016).
31. Hemsing, E., Stupakov, G., Xiang, D. & Zholents, A. Beam by design: laser manipulation of electrons in modern accelerators. *Rev. Mod. Phys.* **86**, 897–941 (2014).
32. Ferrari, E. et al. Widely tunable two-colour seeded free-electron laser source for resonant-pump resonant-probe magnetic scattering. *Nat. Commun.* **7**, 10343 (2015).
33. Hara, T. et al. Two-colour hard X-ray free-electron laser with wide tunability. *Nat. Commun.* **4**, 2919 (2013).
34. Marinelli, A. et al. High-intensity double-pulse X-ray free-electron laser. *Nat. Commun.* **6**, 6369 (2015).
35. Ronsivalle, C. et al. Large-bandwidth two-color free-electron laser driven by a comb-like electron beam. *New J. Phys.* **16**, 033018 (2014).
36. Malka, V. Laser plasma accelerators. *Phys. Plasmas* **19**, 055501 (2012).
37. Corde, S. et al. Observation of longitudinal and transverse self-injections in laser-plasma accelerators. *Nat. Commun.* **4**, 1501 (2013).
38. Mirzaie, M. et al. Demonstration of self-truncated ionization injection for GeV electron beams. *Sci. Rep.* **5**, 14659 (2015).
39. Walker, P. A. et al. Investigation of GeV-scale electron acceleration in a gas-filled capillary discharge waveguide. *New J. Phys.* **15**, 045024 (2013).
40. Lundh, O., Rechatin, C., Lim, J., Malka, V. & Faure, J. Experimental measurements of electron-bunch trains in a laser-plasma accelerator. *Phys. Rev. Lett.* **110**, 065005 (2013).
41. Zeng, M. et al. Multichromatic narrow-energy-spread electron bunches from laser-wakefield acceleration with dual-color lasers. *Phys. Rev. Lett.* **114**, 084801 (2015).
42. Faure, J. et al. Controlled injection and acceleration of electrons in plasma wakefields by colliding laser pulses. *Nature* **444**, 737–739 (2006).
43. Schmid, K. et al. Density-transition based electron injector for laser driven wakefield accelerators. *Phys. Rev. Accel. Beams* **13**, 091301 (2010).
44. Buck, A. et al. Shock-front injector for high-quality laser-plasma acceleration. *Phys. Rev. Lett.* **110**, 185006 (2013).
45. Fubiani, G., Esarey, E., Schroeder, C. B. & Leemans, W. P. Beat wave injection of electrons into plasma waves using two interfering laser pulses. *Phys. Rev. E* **70**, 016402 (2004).
46. Davoine, X., Lefebvre, E., Rechatin, C., Faure, J. & Malka, V. Cold optical injection producing monoenergetic, multi-GeV electron bunches. *Phys. Rev. Lett.* **102**, 065001 (2009).
47. Lehe, R., Lifschitz, A. F., Davoine, X., Thaury, C. & Malka, V. Optical transverse injection in laser-plasma acceleration. *Phys. Rev. Lett.* **111**, 085005 (2013).
48. Lu, W. et al. Generating multi-GeV electron bunches using single stage laser wakefield acceleration in a 3D nonlinear regime. *Phys. Rev. Accel. Beams* **10**, 061301 (2007).
49. Rechatin, C. et al. Controlling the phase-space volume of injected electrons in a laser-plasma accelerator. *Phys. Rev. Lett.* **102**, 164801 (2009).
50. Thomas, A. G. R. Scalings for radiation from plasma bubbles. *Phys. Plasmas* **17**, 056798 (2010).
51. Fubiani, G., Esarey, E., Schroeder, C. B. & Leemans, W. P. Improvement of electron beam quality in optical injection schemes using negative plasma density gradients. *Phys. Rev. E* **73**, 026402 (2006).
52. Xu, J. et al. Dynamics of electron injection in a laser-wakefield accelerator. *Phys. Plasmas* **24**, 083106 (2017).
53. Heigoldt, M. et al. Temporal evolution of longitudinal bunch profile in a laser wakefield accelerator. *Phys. Rev. Accel. Beams* **18**, 121302 (2015).
54. He, Z. H. et al. Capturing structural dynamics in crystalline silicon using chirped electrons from a laser wakefield accelerator. *Sci. Rep.* **6**, 36224 (2016).
55. Gauduel, Y. A., Glinec, Y., Rousseau, J. P., Burgy, F. & Malka, V. High energy radiation femtochemistry of water molecules: early electron-radical pairs processes. *Eur. Phys. J. D* **60**, 121–135 (2010).
56. Petrillo, V. et al. Dual color X rays from Thomson or Compton sources. *Phys. Rev. Accel. Beams* **17**, 020706 (2014).
57. Kalmykov, S. Y., Davoine, X., Ghebregziabher, I. & Shadwick, B. A. Customizable electron beams from optically controlled laser plasma acceleration for γ -ray sources based on inverse Thomson scattering. *Nucl. Instrum. Methods Phys. Res. A* **829**, 52–57 (2016).
58. Kalmykov, S. Y., Davoine, X., Ghebregziabher, I. & Shadwick, B. A. Optically controlled laser–plasma electron accelerator for compact gamma-ray sources. *New J. Phys.* **20**, 023047 (2018).
59. Corde, S. et al. Femtosecond X rays from laser-plasma accelerators. *Rev. Mod. Phys.* **85**, 1–48 (2013).
60. Rykovanov, S. G., Geddes, C. G. R., Schroeder, C. B., Esarey, E. & Leemans, W. P. Controlling the spectral shape of nonlinear Thomson scattering with proper laser chirping. *Phys. Rev. Accel. Beams* **19**, 1039 (2016).
61. Ta Phuoc, K. et al. All-optical Compton gamma-ray source. *Nat. Photon.* **6**, 308–311 (2012).
62. Thomas, A. G. R. et al. Measurements of wave-breaking radiation from a laser-wakefield accelerator. *Phys. Rev. Lett.* **98**, 054802 (2007).
63. Blumenfeld, I. et al. Energy doubling of 42 GeV electrons in a metre-scale plasma wakefield accelerator. *Nature* **445**, 741–744 (2007).
64. Döpp, A. et al. Energy-chirp compensation in a laser wakefield accelerator. *Phys. Rev. Lett.* **121**, 074802 (2018).
65. Manahan, G. G. et al. Single-stage plasma-based correlated energy spread compensation for ultrahigh 6D brightness electron beams. *Nat. Commun.* **8**, 15705 (2017).
66. Rechatin, C. et al. Observation of beam loading in a laser–plasma accelerator. *Phys. Rev. Lett.* **103**, 194804 (2009).
67. Hidding, B. et al. Monoenergetic energy doubling in a hybrid laser-plasma wakefield accelerator. *Phys. Rev. Lett.* **104**, 195002 (2010).
68. Sundström, V. Femtobiology. *Annu. Rev. Phys. Chem.* **59**, 53–77 (2008).
69. Zewail, A. H. Femtochemistry: atomic-scale dynamics of the chemical bond. *J. Phys. Chem. A* **104**, 5660–5694 (2000).
70. Ullrich, J., Rudenko, A. & Moshhammer, R. Free-electron lasers: new avenues in molecular physics and photochemistry. *Annu. Rev. Phys. Chem.* **63**, 635–660 (2012).

Acknowledgements

This work was supported by DFG through the Cluster of Excellence Munich-Centre for Advanced Photonics (MAP EXC 158), DFG-Project Transregio TR-18 funding schemes, by EURATOM-IPP and the Max-Planck-Society. L.V. acknowledges the support by a grant from the Swedish Research Council (2016-05409). The authors thank F. Krausz for helpful comments. A.D. thanks I. Andriyash (WIS) for support with Chimera.

Author contributions

A.B., M.H., K.K., J.W., J.X., L.V. and S.K. performed the experiments with ATLAS-60 at the MPQ. A.D., H.D., M.F.G., J.G., S.S. and S.K. performed the experiments with the upgraded laser system at LEX Photonics. A.D., K.K., S.S. and J.W. analysed the experimental data. A.D. performed PIC simulations, radiation and beam transport calculations. A.D., W.H., K.K., J.W., L.V. and S.K. discussed the results. A.D., K.K. and J.W. wrote the paper. S.K. supervised the project.

Competing interests

The authors declare no competing interests.

Additional information

Supplementary information is available for this paper at <https://doi.org/10.1038/s41566-019-0356-z>.

Reprints and permissions information is available at www.nature.com/reprints.

Correspondence and requests for materials should be addressed to A.D. or S.K.

Publisher's note: Springer Nature remains neutral with regard to jurisdictional claims in published maps and institutional affiliations.

© The Author(s), under exclusive licence to Springer Nature Limited 2019

Methods

Laser systems. The first series of experiments demonstrating low-energy electrons (<40 MeV) were performed using the ATLAS Ti:Sapphire laser at the MPI for Quantum Optics (MPQ), which delivered laser pulses with 1.5 J energy within 28 fs duration (50 TW), centred at 800 nm wavelength. The main part of the laser (1.2 J) has been focused with an F/13 off-axis parabolic mirror reaching an intensity of $1.3 \times 10^{19} \text{ W cm}^{-2}$ ($a_0 = 2.5$) in a focal spot of $(11 \times 12) \mu\text{m}^2$ at $\sim 1.5 \text{ mm}$ above the nozzle exit. For colliding-pulse injection, a small part of the beam containing $\sim 0.3 \text{ J}$ has been cut off by a pick-up mirror in the experimental chamber and was focused by an F/26 off-axis parabolic mirror. For perfect beam overlap, this would result in a peak potential of up to $a_1 \approx 0.9$. However, the actual intensity during the pulse interaction is expected to be much lower, because during alignment we do not optimize towards highest overlap (as in experiments on Thomson backscattering²¹), but for best energy spread and stability of the optically injected electron bunch.

High-energy experiments have been carried out with the upgraded ATLAS laser system, situated at the Laboratory for Extreme Photonics (LEX) at Ludwig-Maximilians University of Munich (LMU), which delivered up to 2.5 J pulses of similar duration ($\sim 80 \text{ TW}$). The pulses were focused on the gas target in a F/25 geometry to a peak intensity of $5.5 \times 10^{18} \text{ W cm}^{-2}$, while the colliding pulse had the same parameters as in the first experiment.

Gas targets and diagnostics. In the first experiments, the gas target was a 300 μm supersonic gas nozzle of de Laval geometry. The shock front was realized by introducing a razor blade perpendicular to the gas flow (Fig. 1). In the second experiment, a larger 5 mm nozzle was used in conjunction with an adjustable silicon wafer. The density profile is characterized using both interferometry and few-cycle shadowgraphy (in the second experiment). The electron energy was characterized using dipole magnet spectrometers. During the first experiment, a magnet spectrometer consisting of a 0.91 T permanent magnet, resolving electron energies from 2.5 MeV to 400 MeV (ref. ⁷¹). In the second experiment, an 80 cm permanent magnet (0.85 T) was used, measuring electron energies from 50 MeV onwards. The plasma mirror for all-optical Compton backscattering is generated using a 15- μm -thick oxide-coated Mylar tape⁷². The emitted radiation was detected using a $\text{Gd}_2\text{O}_2\text{S:Tb}$ scintillator, which is fibre coupled to an MCP-based image intensifier and whose amplified signal is coupled to a CCD sensor⁷³. Note that the intensifier leads to a decrease in image resolution.

PIC simulations. The simulations were performed with the quasi-three-dimensional code CALDER-CIRC⁷⁴, using the two modes $m=0$ and $m=1$ for modelling of the laser and wakefield. The resolution chosen for the parameter scan was $\Delta x = 0.25 k_0^{-1}$, $\Delta r = 1.0 k_0^{-1}$ and 40 particles per cell ($k_0^{-1} = \lambda_0 / 2\pi \approx 127 \text{ nm}$). The laser driver is initialized with a peak potential $a_0 = 2.5$ and a spot size of 12 μm , whereas the collider has an intensity $a_1 = 0.3$. As the density transition length was not directly measured in the first experiment, a plasma gradient length similar to Swanson et al.⁷⁵ was chosen ($75 \mu\text{m} \sim 3.5 \lambda_0$). A total of 40 PIC simulations were performed for the parameter scan shown in Fig. 3. We note that some experiments suggest an even shorter transition length⁵². For this case, simulations still show the same three regimes of operation, but the final energy spread is higher because of accumulated energy chirp at the end of the simulation.

Radiation modelling. Synchrotron radiation was calculated using Chimera⁷⁶. For this, the measured electron spectra were modelled using 10^4 test particles, assuming an FWHM beam divergence of 1 mrad. For undulator simulations, the parameters from Fuchs et al.²⁰ were used, that is $K=0.55$, $N=60$ and $\lambda_u = 5 \text{ mm}$. As the exact experimental parameters of the $\lambda_0 = 800 \text{ nm}$ scattering pulse for the all-optical Compton source could not be measured in our setup, we used PIC simulations to estimate the normalized peak potential at the end of the gas target ($a_0 \sim 2$). Taking into account the reflectance of the plasma mirror (~ 0.5), we chose $a_0 = 1.5$ as estimation for the scattering parameter. The duration is assumed as 30 fs FWHM. To generate the simulated beam profiles, the average electron spectra of ten shots each were used to calculate the energy-dependent far-field emission. In this case, a divergence of 1.5 mrad was used for the low-energy beam and the detector was modelled based on its quantum efficiency.

Beam transport model. The delay in a magnetic chicane presented in Fig. 4d is calculated based on matrix transport elements for ideal dipole magnets and velocity delay in a C-type chicane consisting of four 5-cm-long dipole magnets with varying field strength and two 5-cm-long drifts between the magnets. For the first electron beam (343 MeV), we calculate a linear transport matrix element $R_{56} = -(3.2-39) \mu\text{m}$ and a second-order matrix element $T_{566} = 4.8-58 \mu\text{m}$ at 100–350 mT field strength. For the second bunch (185 MeV), $R_{56} = -11-134 \mu\text{m}$ and $T_{566} = 16.4-201 \mu\text{m}$. For the FWHM energy spreads of both beams (5.8% for the high-energy bunch and 12.8% for the low-energy bunch) this corresponds to a bunch lengthening of 0.6–6.9 fs and 3.8–46.0 fs, respectively. Electron beam divergence is neglected in these calculations since the pulse broadening is negligible (0.5 fs for $L_{\text{chicane}} = 30 \text{ cm}$).

Data availability

The data that support the plots within this paper and other findings of this study are available from the corresponding authors upon reasonable request.

References

- Sears, C. M. S. et al. A high resolution, broad energy acceptance spectrometer for laser wakefield acceleration experiments. *Rev. Sci. Instrum.* **81**, 073304 (2010).
- Shaw, B. H., Steinke, S., van Tilborg, J. & Leemans, W. P. Reflectance characterization of tape-based plasma mirrors. *Phys. Plasmas* **23**, 063118 (2016).
- Götzfried, J. et al. Research towards high-repetition rate laser-driven X-ray sources for imaging applications. *Nucl. Instrum. Methods Phys. Res. A* **909**, 1–4 (2018).
- Lifschitz, A. et al. Particle-in-cell modelling of laser-plasma interaction using Fourier decomposition. *J. Comput. Phys.* **228**, 1803–1814 (2009).
- Swanson, K. K. et al. Control of tunable, monoenergetic laser-plasma-accelerated electron beams using a shock-induced density downramp injector. *Phys. Rev. Accel. Beams* **20**, 051301 (2017).
- Andriyash, I. A., Lehe, R. & Malka, V. A spectral unaveraged algorithm for free electron laser simulations. *J. Comput. Phys.* **282**, 397–409 (2015).